

Projection Method for Incompressible Flow

Knut Sverdrup

Abstract

In this report, we discuss computational methods for solving the incompressible Navier-Stokes equations in the two-dimensional test case of a lid-driven cavity. For Newtonian fluids, we demonstrate the implementation of a fractional-step projection method for solving the transient problem with moderately high Reynolds numbers, and show that the system converges to the steady-state solution previously documented in the literature. Additionally, we discuss the case of Reynolds number zero in Bingham plastic fluids, and how the steady-state solution can be computed through the SIMPLE algorithm when regularization is employed to deal with the singularity in apparent viscosity of such fluids.

1. Introduction

In physics, few equations span as wide a range of applications as the Navier-Stokes equations of fluid dynamics. They govern the motion of viscous fluids in a continuum framework, and as such have applications in e.g. climate modelling^[1,2], aerodynamics^[3–5], medicinal research^[6,7] and petroleum engineering^[8–11], to name a few. Named after Claude Navier and George Stokes for their major contributions^[12,13] to its formulation in the first half of the nineteenth century, the equations have constituted a major field of research in their own right since their formulation, and continue to do so today. Apart from their numerous applications, the equations are fundamentally interesting from a mathematical point of view. In fact, (dis-)proving the existence and uniqueness of their solutions is one of the seven Millenium prize problems^[14] for which a prize of one million US dollars is associated.

The generalized Navier-Stokes equations are based on the conservation of mass through the continuity equation,

$$\partial_t \rho + \nabla \cdot (\rho \mathbf{u}) = 0, \quad (1)$$

in addition to conservation of momentum as given by the Cauchy momentum equation

$$\rho (\partial_t \mathbf{u} + \mathbf{u} \cdot \nabla \mathbf{u}) = -\nabla p + \nabla \cdot \boldsymbol{\tau} + \mathbf{f}. \quad (2)$$

Here, we have introduced the primitive variables density ρ , velocity \mathbf{u} and pressure p , in addition to

the deviatoric stress tensor $\boldsymbol{\tau}$. The vector \mathbf{f} accounts for external body sources such as gravity acting on the fluid, and shall henceforth be disregarded. The Navier-Stokes equations are an extension of Eqns. (1) and (2) derived under the assumptions that the stress tensor $\boldsymbol{\tau}$ is a linear function of the strain tensor $\dot{\boldsymbol{\gamma}} = \nabla \mathbf{u} + (\nabla \mathbf{u})^T$, that $\nabla \cdot \boldsymbol{\tau} = 0$ for fluids at rest, and that the fluid is isotropic. Given these assumptions, Eq. (2) can be rewritten

$$\rho (\partial_t \mathbf{u} + \mathbf{u} \cdot \nabla \mathbf{u}) = -\nabla p + \nabla \cdot (\mu \dot{\boldsymbol{\gamma}}) + \nabla (\lambda \nabla \cdot \mathbf{u}) \quad (3)$$

where μ and λ are the first and second coefficients of viscosity, respectively. Fluids which obey the Navier-Stokes equations as given by Eqns. (1) and (3) are labelled Newtonian fluids. The second coefficient of viscosity, λ , is related to bulk viscosity and disappears for incompressible flow, which we restrict ourselves to in this project. Consequently, we simply refer to μ as the viscosity of the fluid.

When the density, ρ , is constant within each control volume of the fluid, the flow is said to be isochoric or incompressible. A vast amount of cases in continuum mechanics relate to incompressible flow, and several simplifications arise in the description of the fluid. Firstly, Eq. (1) reduces to the incompressibility constraint

$$\nabla \cdot \mathbf{u} = 0. \quad (4)$$

Secondly, the viscosity μ is constant for incompressible flow. Consequently, Eq. (3) simplifies to

$$\rho(\partial_t \mathbf{u} + \mathbf{u} \cdot \nabla \mathbf{u}) = -\nabla p + \mu \nabla^2 \mathbf{u}, \quad (5)$$

where we have used the fact that $\nabla \cdot \dot{\gamma} = \nabla^2 \mathbf{u}$ for incompressible flow. Eqns. (4) and (5) make up the incompressible Navier-Stokes equations for incompressible flow.

In order to nondimensionalize our system of equations, we move to dimensionless variables such that $\mathbf{u} \rightarrow \frac{1}{a} \mathbf{u}$, $\partial_t \rightarrow \frac{L}{a} \partial_t$ and $\nabla \rightarrow L \nabla$, where L is the length of the system under consideration and a is the maximum absolute value of the velocity. Applying these changes to Eq. (5) and multiplying through by $L/\rho a^2$ gives the dimensionless equation

$$\partial_t \mathbf{u} + \mathbf{u} \cdot \nabla \mathbf{u} = -\frac{1}{\text{Re}} \nabla p + \frac{1}{\text{Re}} \nabla^2 \mathbf{u}. \quad (6)$$

Here, $\text{Re} = \rho a L / \mu$ is the Reynolds number of the flow, which equals the ratio of inertial forces to viscous ones. Note that the pressure is still measured in physical units, as we wish to utilize different scalings depending on the Reynolds number. Low Reynolds numbers correspond to laminar flow, where the viscous forces are dominant. In this case, we let $p \rightarrow \frac{\text{Re}}{\rho a^2} p$, so that Eq. (6) becomes

$$\text{Re}(\partial_t \mathbf{u} + \mathbf{u} \cdot \nabla \mathbf{u}) = -\nabla p + \nabla^2 \mathbf{u}. \quad (7)$$

High Reynolds numbers, on the other hand, correspond to turbulent flow with the most important contributions arising from the inertial forces. We then let $p \rightarrow \frac{1}{\rho a^2} p$, yielding the alternative formulation

$$\partial_t \mathbf{u} + \mathbf{u} \cdot \nabla \mathbf{u} = -\nabla p + \frac{1}{\text{Re}} \nabla^2 \mathbf{u}. \quad (8)$$

In our implementation of fractional step projection methods for incompressible flow of Newtonian fluids, Eq. (8) is the formulation of interest. When discussing creeping flow for Bingham plastic fluids, however, we return to (a variant of) Eq. (7).

Several models exist to describe different types of Non-Newtonian fluids, each characterized by the way the stress $\tau = \sqrt{\frac{1}{2} \sum \tau_{i,j}^2}$ depends on the strain rate $\dot{\gamma} = \sqrt{\frac{1}{2} \sum \dot{\gamma}_{i,j}^2}$. The interesting quantity is the apparent viscosity $\eta = \tau / \dot{\gamma}$. For Newtonian fluids, as we have already seen, the relationship is linear, with slope $\eta = \mu$. Non-Newtonian fluids include dilatants (shear-thickening, $\partial \eta / \partial \dot{\gamma} > 0$) and pseudoplastics (shear-thinning, $\partial \eta / \partial \dot{\gamma} < 0$), but in this project we restrict ourselves to the relatively simple

case of Bingham plastics. Figure 1 illustrates the different types of fluids.

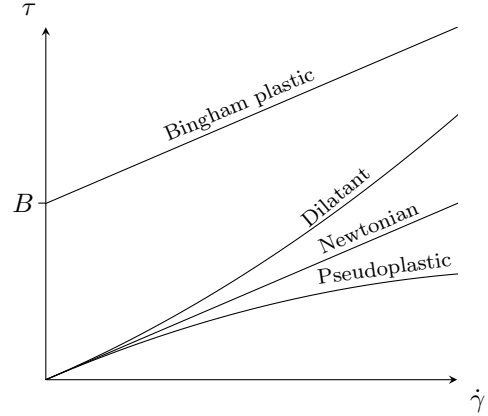


Figure 1: Classification of fluids based on apparent viscosity.

Bingham plastic fluids, named after Eugene Cook Bingham for his investigation into them in 1916^[15], have a threshold stress τ_0 , below which they do not yield to applied forces. For the nondimensionalized stress tensor, the yield stress corresponds to the dimensionless Bingham number $B = \tau_0 L / \mu a$. In other words, the strain rate is zero unless a stress higher than that characteristic stress is applied. Physically, this means that they behave as solids for small stresses, something which leads to interesting behaviour such as non-flat surfaces at rest. This can be demonstrated by distorting the surface of a mayonnaise container: gravity alone is not strong enough to surpass the yield stress, and the surface remains in its distorted state. Regions where the flow is such that $\tau < B$ are also known as unyielded regions. The relationship between stress and shear rate for Bingham plastics is therefore

$$\dot{\gamma} = \begin{cases} 0, & \tau \leq B \\ \tau - B, & \tau > B \end{cases}, \quad (9)$$

from which it is evident that the apparent viscosity

$$\eta = \frac{B}{\dot{\gamma}} + 1, \quad (10)$$

and as such has a singularity for $\dot{\gamma} = 0$.

As a test framework for our numerical schemes, we apply them to the so-called lid-driven cavity problem. The problem has served as a benchmark test for viscous, incompressible fluid flow for decades, and reference solutions are readily available, notably those produced by Ghia et al. in 1982

through the vorticity-stream function formulation and multigrid methods^[16]. This test case is fairly simple, and consists of a square domain in two dimensions with sides of length L . At all sides, both solid-wall and no-slip boundary conditions are applied, so that the component of $\mathbf{u} = (u, v)^T$ normal to the wall is zero on the whole boundary, while the tangential component equals the velocity of wall. In the lid-driven cavity test, all walls are stationary except the top one (the “lid”), which moves with constant speed a . Figure 2 exhibits the test case schematically.

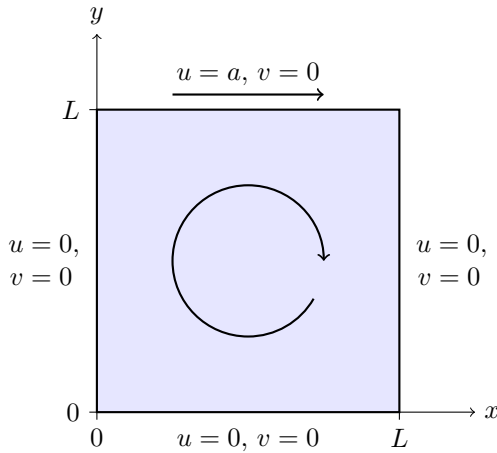


Figure 2: Lid-driven cavity test case.

In Section 2, the numerical methods employed to solve the incompressible Navier-Stokes equations for Newtonian fluids in the lid-driven cavity are explained. In addition to this, the extensions needed to simulate creeping flow of Bingham plastics are discussed. Section 3 contains our results with accompanying comments. Suggestions for possible extensions are given in Section 4, while Section 5 concludes the report.

2. Numerical methods

2.1. Newtonian fluid

For the case of a Newtonian fluid, our aim is to find the solution of the unsteady (transient) Navier-Stokes equations. The coupling of the velocity and pressure poses a difficulty however, and must be approached in a manner which allows consistent discretization in time. Subsequently, the spatial domain must be considered, and the resulting systems

of equations solved. We presently explain the chosen techniques to do so, and include notes on how they have been implemented.

2.1.1. Projection method

In order to solve the transient problem given by Eqns. (8) and (4), we implement a fractional-step projection method following section 10.3 of Oleg Zikanov’s *Essential Computational Fluid Dynamics*^[17]. The original projection method for Navier-Stokes equations was invented by Chorin in 1968^[18], and the essence is still the same in modern variants. It is an operator splitting approach, in which, for each time step, one first performs an intermediate time step while ignoring the pressure forces, and then ignores the viscous forces in the second time step. Temporal discretization of Eq.(8) is done explicitly for the nonlinear term and implicitly for the linear ones, yielding the two equations

$$\frac{\tilde{\mathbf{u}}^{n+1} - \mathbf{u}^n}{\Delta t} + \mathbf{u}^n \cdot \nabla \mathbf{u}^n - \frac{1}{\text{Re}} \nabla^2 \tilde{\mathbf{u}}^{n+1} = 0, \quad (11)$$

$$\frac{\mathbf{u}^{n+1} - \tilde{\mathbf{u}}^{n+1}}{\Delta t} + \nabla p^{n+1} = 0, \quad (12)$$

which reduce to the discrete version of Eq. (8) when added together. Here, we have introduced the notation $\mathbf{u}^n = \mathbf{u}(n\Delta t)$, in addition to denoting by $\tilde{\mathbf{u}}^{n+1}$ the velocity at the intermediate time step. It is particularly important to utilize the implicit temporal discretization for flows with low Reynolds numbers and for meshes that are stretched near boundaries, because otherwise the numerical viscous stability restriction becomes severe in these cases.

Given a suitable spatial discretization scheme, Eq. (11) is straightforward to solve since there are two known (\mathbf{u}^n) and two unknown ($\tilde{\mathbf{u}}^{n+1}$) quantity. The second step, however, has two unknowns. This problem is solved by taking the divergence of Eq.(12) and enforcing $\nabla \cdot \mathbf{u}^{n+1} = 0$, leading to a Poisson equation for the pressure:

$$\nabla^2 p^{n+1} = \frac{1}{\Delta t} \nabla \cdot \tilde{\mathbf{u}}^{n+1}. \quad (13)$$

By doing so, the intermediate, unphysical velocity, which was computed without enforcing incompressibility, is projected onto the space of vector fields satisfying Eq. (4).

The velocity at time t^{n+1} can finally be updated by rearranging Eq. (12) to read

$$\mathbf{u}^{n+1} = \tilde{\mathbf{u}}^{n+1} + \Delta t \nabla p^{n+1}. \quad (14)$$

2.1.2. Finite volumes

Spatial discretization is done through finite volumes with a staggered grid, i.e. a grid where the three primitive variables are evaluated at different points. The need for a staggered grid is due to the relationship between pressure and velocity. On a regular grid, a checkerboard pattern occurs in their dependencies upon each other, leading to decoupling and thus spurious pressure instabilities. Our domain is split into N equal subdomains for pressure in each spatial direction, leading to a total of N^2 subdomains of area Δx^2 , where $\Delta x = 1/N$ (we employ the same grid spacing in both directions). In the centre of each of these squares, the pressure is evaluated, while the x - and y -components of velocity are evaluated on their vertical and horizontal borders, respectively. Consequently, the control volumes for the first and second components of the momentum balance equations in the finite volume method are shifted by $\frac{1}{2}\Delta x$ compared to the control volumes used for the Poisson equation for pressure. The staggered grid with shifted control volumes is illustrated in Figure 3.

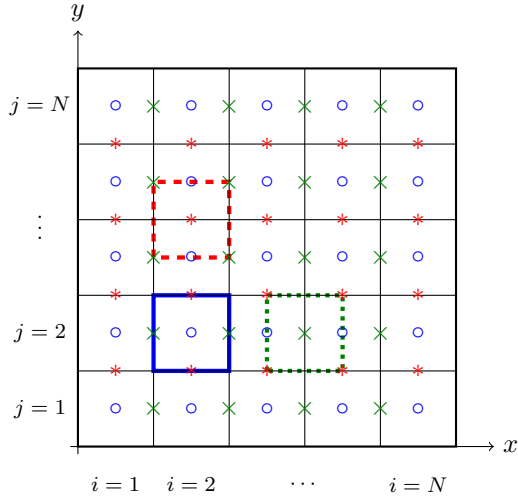


Figure 3: Spatial discretization of the square domain with a staggered grid. At the different points, the primitive variables are evaluated: \circ p , \times u , $*$ v . Examples of control volumes for pressure ($i = 2, j = 2$), x -velocity ($i = 3.5, j = 2$) and y -velocity ($i = 2, j = 2.5$) are also shown with corresponding colors. In this example, $N = 5$.

We denote by $\Omega_{i,j}$ the control volume centred at $(x_i, y_j) = (i\Delta x - 1/2, j\Delta x - 1/2)$. In integral form over a control volume centred at a u -point, the first component of Eq. (11) reads

$$\begin{aligned} & \int_{\Omega_{i+\frac{1}{2},j}} \tilde{u}^{n+1} dV - \frac{\Delta t}{\text{Re}} \int_{\Omega_{i+\frac{1}{2},j}} \nabla^2 \tilde{u}^{n+1} dV \\ &= \int_{\Omega_{i+\frac{1}{2},j}} u^n dV + \Delta t \int_{\Omega_{i+\frac{1}{2},j}} (u^n \partial_x u^n + v^n \partial_y u^n) dV. \end{aligned} \quad (15)$$

We approximate the first term on each side of the equation by the two-dimensional midpoint rule, i.e.

$$\int_{\Omega_{i+\frac{1}{2},j}} \tilde{u}^{n+1} dV \approx \tilde{u}_{i+\frac{1}{2},j}^{n+1} (\Delta x)^2, \quad (16)$$

and similar for u^n . Derivatives are approximated by central differences, and when evaluation of a variable is necessary at a point where it is not defined, the mean value of the nearest neighbours to the point is taken instead. Thus, the integral in the term with the Laplacian becomes

$$\begin{aligned} & \int_{\Omega_{i+\frac{1}{2},j}} \nabla^2 \tilde{u}^{n+1} dV = \int_{\partial\Omega_{i+\frac{1}{2},j}} \partial_n \tilde{u}^{n+1} dS \\ & \approx \tilde{u}_{i+\frac{3}{2},j}^{n+1} + \tilde{u}_{i+\frac{1}{2},j-1}^{n+1} + \tilde{u}_{i-\frac{1}{2},j}^{n+1} + \tilde{u}_{i+\frac{1}{2},j+1}^{n+1} - 4\tilde{u}_{i+\frac{1}{2},j}^{n+1}, \end{aligned} \quad (17)$$

while the integrals in the nonlinear term are approximated as

$$\int_{\Omega_{i+\frac{1}{2},j}} u^n \partial_x u^n dV \approx u_{i+\frac{1}{2},j}^n \frac{1}{2} (u_{i+\frac{3}{2},j}^n - u_{i-\frac{1}{2},j}^n) \Delta x, \quad (18)$$

$$\begin{aligned} & \int_{\Omega_{i+\frac{1}{2},j}} v^n \partial_y u^n dV \approx \frac{1}{2} (u_{i+\frac{1}{2},j+1}^n - u_{i+\frac{1}{2},j-1}^n) \Delta x \\ & \times \frac{1}{4} (v_{i+1,j+\frac{1}{2}}^n + v_{i+1,j-\frac{1}{2}}^n + v_{i,j-\frac{1}{2}}^n + v_{i,j+\frac{1}{2}}^n). \end{aligned} \quad (19)$$

By substituting the approximations in Eqns. (16) - (19) in Eq. (15), we arrive at a matrix equation of the form

$$A_{uv} \tilde{\mathbf{u}} = \mathbf{f}_u + \mathbf{b}_u, \quad (20)$$

where A_{uv} is an $N(N-1) \times N(N-1)$ matrix, $\tilde{\mathbf{u}}$ is a vector containing the discrete values of \tilde{u}^{n+1} at each point and \mathbf{f}_u is a load vector depending only

on values of \mathbf{u} and \mathbf{v} at the previous time step.¹ The vector \mathbf{b}_u takes into consideration the boundary conditions, and will be treated shortly. The matrix is a sparse block tridiagonal matrix of the form

$$A_{uv} = \begin{pmatrix} I - \alpha B & -\alpha I & & \\ -\alpha I & I - \alpha B & -\alpha I & \\ & & \ddots & \\ & & -\alpha I & I - \alpha B \end{pmatrix},$$

where $\alpha = \frac{\Delta t}{\text{Re}(\Delta x)^2}$, I is the identity matrix and

$$B = \begin{pmatrix} -4 & 1 & & \\ 1 & -4 & 1 & \\ & & \ddots & \\ & & 1 & -4 \end{pmatrix}.$$

By the exact same procedure for the second component of Eq. (11), using control volumes $\Omega_{i,j+\frac{1}{2}}$, one arrives at a similar equation for the intermediate y -velocities:

$$A_{uv} \tilde{\mathbf{v}} = \mathbf{f}_v + \mathbf{b}_v, \quad (21)$$

By comparison, the spatial discretization of Eq. (13) is straightforward. In discrete form over a control volume, it reads

$$\int_{\Omega_{i,j}} \nabla^2 p^{n+1} dV = \frac{1}{\Delta t} \int_{\Omega_{i,j}} \nabla \cdot \tilde{\mathbf{u}}^{n+1} dV. \quad (22)$$

We discretize the pressure term as

$$\begin{aligned} \int_{\Omega_{i,j}} \nabla^2 p^{n+1} dV &= \int_{\partial\Omega_{i,j}} \nabla p^{n+1} \cdot d\mathbf{S} \\ &\approx p_{i+1,j}^{n+1} + p_{i,j-1}^{n+1} + p_{i-1,j}^{n+1} + p_{i,j+1}^{n+1} - 4p_{i,j}^{n+1}, \end{aligned} \quad (23)$$

while the term containing the intermediate velocity becomes

$$\begin{aligned} \int_{\Omega_{i,j}} \nabla \cdot \tilde{\mathbf{u}}^{n+1} dV &= \int_{\partial\Omega_{i,j}} \tilde{\mathbf{u}}^{n+1} \cdot d\mathbf{S} \\ &\approx (\tilde{u}_{i+\frac{1}{2},j}^{n+1} - \tilde{u}_{i-\frac{1}{2},j}^{n+1} + \tilde{v}_{i,j+\frac{1}{2}}^{n+1} - \tilde{v}_{i,j-\frac{1}{2}}^{n+1}) \Delta x. \end{aligned} \quad (24)$$

¹Note that bold symbols in italics refer to physical variables such as $\mathbf{u} = (u, v)^T$, while roman bold symbols are vectors of discrete values, e.g. $\mathbf{u} = \{u_{i+\frac{1}{2},j}\}$ for $i \in \{1, 2, \dots, N-1\}$, $j \in \{1, 2, \dots, N\}$.

We thus end up with a system of linear equations:

$$A_p \mathbf{p} = \mathbf{f}_p + \mathbf{b}_p. \quad (25)$$

In this case, there are N^2 variables and unknowns, and the matrix is given by

$$A_p = \begin{pmatrix} B & I & & \\ I & B & I & \\ & & \ddots & \\ & & I & B \end{pmatrix}.$$

2.1.3. Boundary conditions

Special consideration must be taken near the boundaries of the domain. The update formula for an x -momentum control volume requires information taken from the four nearest x -momentum control volumes (north, east, south and west) in addition to the four nearest y -momentum control volumes (northeast, southeast, southwest and northwest). Upon investigation of Figure 3, it is evident that we then need ghost cells for \tilde{u} at $i = 1/2$, $i = N + 1/2$, $j = 0$ and $j = N + 1$. The first two are given immediately by the Dirichlet conditions (no-slip, solid wall), while the latter are computed using interpolation.

$$\begin{aligned} \tilde{u}_{\frac{1}{2},j}^n &= 0, & \tilde{u}_{N+\frac{1}{2},j}^n &= 0, \\ \tilde{u}_{i+\frac{1}{2},0}^n &= -\tilde{u}_{i+\frac{1}{2},1}^n, & \tilde{u}_{i+\frac{1}{2},N+1}^n &= 2a - \tilde{u}_{i+\frac{1}{2},N}^n. \end{aligned} \quad (26)$$

Utilizing the same technique for \tilde{v} , we have

$$\begin{aligned} \tilde{v}_{i,\frac{1}{2}}^n &= 0, & \tilde{v}_{i,N+\frac{1}{2}}^n &= 0, \\ \tilde{v}_{0,j+\frac{1}{2}}^n &= -\tilde{v}_{1,j+\frac{1}{2}}^n, & \tilde{v}_{N+1,j+\frac{1}{2}}^n &= -\tilde{v}_{N,j+\frac{1}{2}}^n. \end{aligned} \quad (27)$$

The boundary conditions for p are less obvious, and have been subject to debate in the literature^[19]. As there are no physical boundary conditions on p , one could take the inner product of Eq. (8) with either the unit normal or unit tangent at the boundary, and retrieve equally feasible boundary conditions. In general, the former is preferred, since the condition relates naturally to the projection operator. Requiring that the space of divergence-free vector fields is orthogonal to the space of irrotational vector fields results in the boundary condition $\mathbf{u}^{n+1} \cdot \mathbf{n} = 0$. Taking the inner product of Eq.

(12) with \mathbf{n} thus gives $\partial_n p = 0$ on the domain border. Our boundary conditions for the pressure are then

$$\begin{aligned} p_{0,j}^{n+1} &= p_{1,j}^{n+1}, & p_{i,0}^{n+1} &= p_{i,1}^{n+1}, \\ p_{N+1,j}^{n+1} &= p_{N,j}^{n+1}, & p_{i,N+1}^{n+1} &= p_{i,N}^{n+1}. \end{aligned} \quad (28)$$

2.1.4. Eigen for systems of equations

Each of the linear systems in Eqns. (20), (21) and (25) are solved using a C++ template library for linear algebra called Eigen^[20]. Since the matrices are sparse, we exploit the special sparse datastructures available in Eigen, and solve the systems using a direct simplicial Cholesky factorization without square root ($A = LDL^T$). The choice of factorization is for efficiency, and can be used since the sparse matrices are Hermitian (self-adjoint) and positive definite.

2.1.5. Stability and convergence to steady-state

An important question in any time-marching scheme for partial differential equations is the restriction on the time step Δt necessary to achieve stability. For a nonlinear scheme such as the one employed, analytical stability restrictions are not available to the best knowledge of the author, but it is still possible to gather some insights from investigating the scheme. The restrictions on Δt are dependent on $\alpha = \frac{\Delta t}{\text{Re}(\Delta x)^2}$ from the diffusive term and $\beta = \frac{\|\mathbf{u}\|_\infty \Delta t}{\Delta x}$ from the convective one. A possibility is therefore to choose Δt as a constant times the minimum of these two restrictors, i.e.

$$\Delta t = C \min \left\{ \frac{\Delta x}{\|\mathbf{u}\|_\infty}, \text{Re}(\Delta x)^2 \right\}. \quad (29)$$

Another approach is to perform stability analysis on a linearized version of the scheme, and transfer the knowledge to the application of the nonlinear method. It has been shown that the general form of the dependency of Δt on Δx , $\|\mathbf{u}\|_\infty$ and Re is predicted only somewhat correctly from this type of procedure^[21].

Since no thorough analysis is possible, we have chosen to do a numerical trial-and-error experiment to find the maximum time step Δt_m which produces stable results for a series of different Reynolds numbers and grid sizes. We can then choose the time step in a manner which ensures that $\Delta t < \Delta t_m$.

If the system converges to steady-state behaviour, the change in the primitive variables will

approach zero. We therefore set a tolerance ϵ and advance the system in time until the relative change in the uniform norm of the vector of discrete velocity values becomes smaller than that tolerance. In other words, we require $\frac{\|\mathbf{u}^{n+1} - \mathbf{u}^n\|_\infty}{\|\mathbf{u}^{n+1}\|_\infty} < \epsilon$ for convergence.

2.1.6. Vorticity and stream function formulation

Our reference solutions are those of Ghia et al.^[16], but their calculations are based on a vorticity and stream function formulation of the 2D Navier-Stokes equations. In order to compare our results more easily, we therefore compute these quantities at the end of the simulation. The scalar stream function ψ is defined for incompressible flow in 2D through the velocity components such that

$$u = \partial_y \psi, \quad v = -\partial_x \psi. \quad (30)$$

The difference between the stream function at two points equals the volumetric flux through a line connecting these points. Contour lines of the stream function are known as stream lines. Stream lines are parallel to the velocity field at all points in the domain, and trace the movement of particles in the fluid. Vorticity, on the other hand, describes the local spinning motion of the fluid at a point. Although a vector quantity in general (the curl of the velocity field), in 2D there is only one non-zero component. We thus define the vorticity as

$$\omega = |\nabla \times \mathbf{u}| = \partial_x v - \partial_y u, \quad (31)$$

which means that computation of the vorticity at grid points $(x_{i+\frac{1}{2}}, y_{j+\frac{1}{2}})$ in our mesh is straightforward given the velocity components. Insertion of Eq. (30) into Eq. (31) gives a simple Poisson equation relating ψ to ω :

$$\omega = -\nabla^2 \psi \quad (32)$$

Conversion from primitive variables to stream function and vorticity can thus be achieved by first calculating the vorticity at each grid point, and subsequently solving Eq. (32) with zero boundary conditions.

2.2. Bingham plastic fluid

Extension of the two-dimensional Navier-Stokes solver to the particular case of Non-Newtonian fluids known as Bingham plastics introduces two difficulties. Firstly, the temporal discretization of the

viscous term is cumbersome. As introduced in Section 1, the viscous term $\nabla^2 \mathbf{u}$ is replaced by $\nabla \cdot \boldsymbol{\tau}$ for these fluids, where

$$\boldsymbol{\tau} = \eta(\dot{\gamma})\dot{\gamma} = \left(\frac{B}{\dot{\gamma}} + 1\right)\dot{\gamma}. \quad (33)$$

It is not possible to discretize this term implicitly in time while retaining the linearity of the system for $\tilde{\mathbf{u}}^{n+1}$. Secondly, the singularity of the apparent viscosity for $\dot{\gamma} = 0$ cannot be handled in a direct manner computationally.

2.2.1. Creeping flow

An idea for circumventing the first of these problems is to discretize the fluid strain rate tensor implicitly while accepting an explicit temporal discretization for the strain rate magnitude in the apparent viscosity, in other words pursuing a discretization such as $\boldsymbol{\tau}^{n+\frac{1}{2}} = \eta(\dot{\gamma}^n)\dot{\gamma}^{n+1}$. This would result in a solvable system of equations. As we restrict ourselves to the case of creeping flows ($\text{Re} = 0$), however, this problem vanishes automatically. Equation (7) applied to the case of Bingham plastic fluids reads

$$\text{Re}(\partial_t \mathbf{u} + \mathbf{u} \cdot \nabla \mathbf{u}) = -\nabla p + \nabla \cdot \eta(\dot{\gamma})\dot{\gamma}, \quad (34)$$

but when $\text{Re} = 0$, the left side of the equation vanishes and we are left with the problem of solving

$$\nabla p = \nabla \cdot \eta(\dot{\gamma})\dot{\gamma} \quad (35)$$

under the incompressibility criterion of Eq. (4). We therefore only make a note that computational solutions exist for Bingham plastics in the transient case (see e.g. Vola et al.^[22] or Muravleva^[23]), and concentrate our efforts on the steady-state case when Eq. (35) is satisfied.

2.2.2. Regularization

In order to deal with the singularity in apparent viscosity, a well-tested technique is regularization. The idea is to replace the discontinuity with a smooth function which mimics its behaviour. One such regularization technique which has been used extensively in the literature^[24–26] is named after Papanastasiou, who authored a paper on it in 1987^[27]. Papanastasiou regularization introduces a parameter m and replaces the apparent viscosity as given by Eq. (10) by the smooth function

$$\eta_p = \frac{B}{\dot{\gamma}} (1 - e^{-m\dot{\gamma}}) + 1 \quad (36)$$

which is well-defined also in the limit as $\dot{\gamma}$ approaches zero. Figure 4 exhibits the behaviour of the function for several values of m . Physically, using Eq. (36) to describe the apparent viscosity corresponds to replacing the “solid” behaviour in the unyielded regions by a fluid with very high viscosity. When choosing the value of the parameter m , it is obviously desirable to make it large, since this mimics the physical apparent viscosity better. On the other hand, the exponential in Eq. (36), when combined with local numerical errors, causes non-smooth lines and zig-zagging behaviour for higher m ^[24].

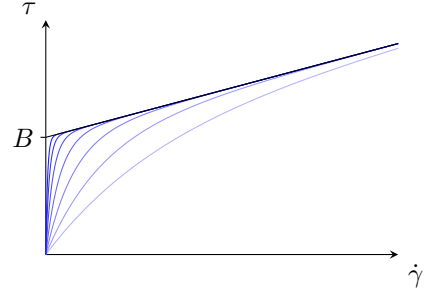


Figure 4: Papanastasiou regularization of the apparent viscosity. The black line corresponds to the physical apparent viscosity, whereas blue uses the Papanastasiou viscosity η_p for various m . Larger values of m are plotted with darker blue.

2.2.3. Spatial discretization

Equation (35) is no longer of the form which produces a checkerboard pattern upon spatial discretization, so there is no longer need for a staggered grid. We therefore use a standard, colocated grid for u , v and p and discretize as before with finite volumes. For each control volume, Eq. (35) in integral form can be written

$$\int_{\partial\Omega_{i,j}} p d\mathbf{S} = \int_{\partial\Omega_{i,j}} \eta\dot{\gamma} \cdot d\mathbf{S}. \quad (37)$$

Discretizing the first component of the pressure term in Eq. (37) is trivial:

$$\int_{\partial\Omega_{i,j}} p d\mathbf{S} \cdot \mathbf{e}_x \approx (p_{i+\frac{1}{2},j} - p_{i-\frac{1}{2},j})\Delta x. \quad (38)$$

The stress is slightly more cumbersome. We note that, in two dimensions, for incompressible flow, the strain rate tensor is given by

$$\dot{\gamma} = \begin{pmatrix} \partial_x u - \partial_y v & \partial_y u + \partial_x v \\ \partial_y u + \partial_x v & \partial_x u - \partial_y v \end{pmatrix}, \quad (39)$$

so that its magnitude is

$$\dot{\gamma} = \sqrt{(\partial_x u - \partial_y v)^2 + (\partial_y u + \partial_x v)^2}. \quad (40)$$

We approximate the derivatives of the velocities on right part of the boundary $\partial\Omega_{i,j}$ by

$$\begin{aligned} \partial_x u_{i+\frac{1}{2},j} &\approx \frac{u_{i+1,j} - u_{i,j}}{\Delta x}, \\ \partial_y u_{i+\frac{1}{2},j} &\approx \frac{u_{i,j+1} + u_{i+1,j+1} - u_{i+1,j-1} - u_{i,j-1}}{4\Delta x}, \\ \partial_x v_{i+\frac{1}{2},j} &\approx \frac{v_{i+1,j} - v_{i,j}}{\Delta x}, \\ \partial_y v_{i+\frac{1}{2},j} &\approx \frac{v_{i,j+1} + v_{i+1,j+1} - v_{i+1,j-1} - v_{i,j-1}}{4\Delta x}, \end{aligned} \quad (41)$$

and similarly for the other edges of the boundary. For brevity, we also denote by $\dot{\gamma}_{i+\frac{1}{2},j}$ the evaluation of Eq. (40) using these approximations. The first component of the viscous term in Eq. (37) can then be approximated as

$$\begin{aligned} \frac{1}{\Delta x} \int_{\partial\Omega_{i,j}} \eta_p \dot{\gamma} \cdot d\mathbf{S} \cdot \mathbf{e}_x \approx & \\ & + \eta_p (\dot{\gamma}_{i+\frac{1}{2},j}) (\partial_x u_{i+\frac{1}{2},j} - \partial_y v_{i+\frac{1}{2},j}) \\ & - \eta_p (\dot{\gamma}_{i-\frac{1}{2},j}) (\partial_x u_{i-\frac{1}{2},j} - \partial_y v_{i-\frac{1}{2},j}) \\ & + \eta_p (\dot{\gamma}_{i,j+\frac{1}{2}}) (\partial_y u_{i,j+\frac{1}{2}} + \partial_x v_{i,j+\frac{1}{2}}) \\ & - \eta_p (\dot{\gamma}_{i,j-\frac{1}{2}}) (\partial_y u_{i,j-\frac{1}{2}} + \partial_x v_{i,j-\frac{1}{2}}). \end{aligned} \quad (42)$$

We thus have a discretized version of the x -component of Eq. (37), and obtain a similar one by exactly the same procedure for the y -component. The only remaining problem is then to solve the nonlinear system of discretized equations.

2.2.4. Projection methods for steady-state flows

A popular algorithm for solving nonlinear systems of the form that arises from our spatial discretization of Eq. (37) is the Semi-Implicit Method for Pressure-Linked Equations (SIMPLE). For a full explanation of the method and versions of it

(SIMPLEC, SIMPLER, ...), we recommend Section 10.4 of Zikanov's book^[17]. The basic idea in these methods is to construct a number of linear systems to be solved iteratively until convergence is achieved. Linearization of the discretized sets of equations is done by computing some terms with values from previous iterations. Successful implementation of the SIMPLE algorithm to solve the steady-state Navier-Stokes equations has been demonstrated in the literature^[25].

3. Results

All results presented in this Section are generated using the implemented scheme described in Subsection 2.1, run on a laptop with an Intel Core i7 CPU 2.50 GHz \times 4 and 16 GB RAM running Linux ubuntu 12.04 LTS. The velocity of the lid is taken to be $a = 1.0$, while the tolerance required for convergence to steady-state is set to $\epsilon = 10^{-5}$.

3.1. Analysis of time step size

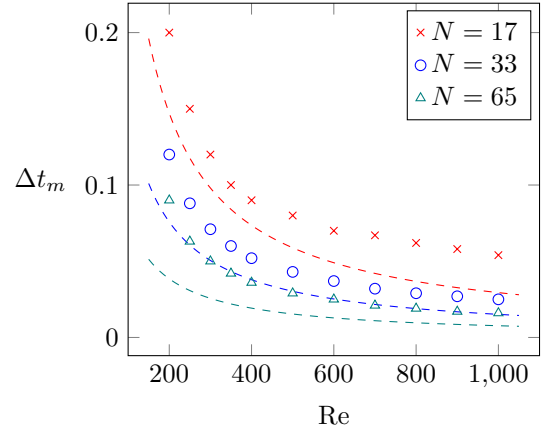


Figure 5: Maximum time step for convergence to steady-state as a function of the Reynolds number. The dashed lines of the same colour as the points correspond to our choice of $\Delta t = 500\Delta x/\text{Re}$.

Figure 5 shows the results from our numerical experiment to determine maximum time step size. As expected, a reduction in temporal step size is required for increases in both Reynolds number and the amount of grid points. Based on this trend, we decided to use a formula of the form $\Delta t \propto \Delta x/\text{Re}$ when choosing the time step. The dashed lines in Figure 5 show corresponding lines with a proportionality factor of 500. With this choice of time step, our simulations remain stable for as large

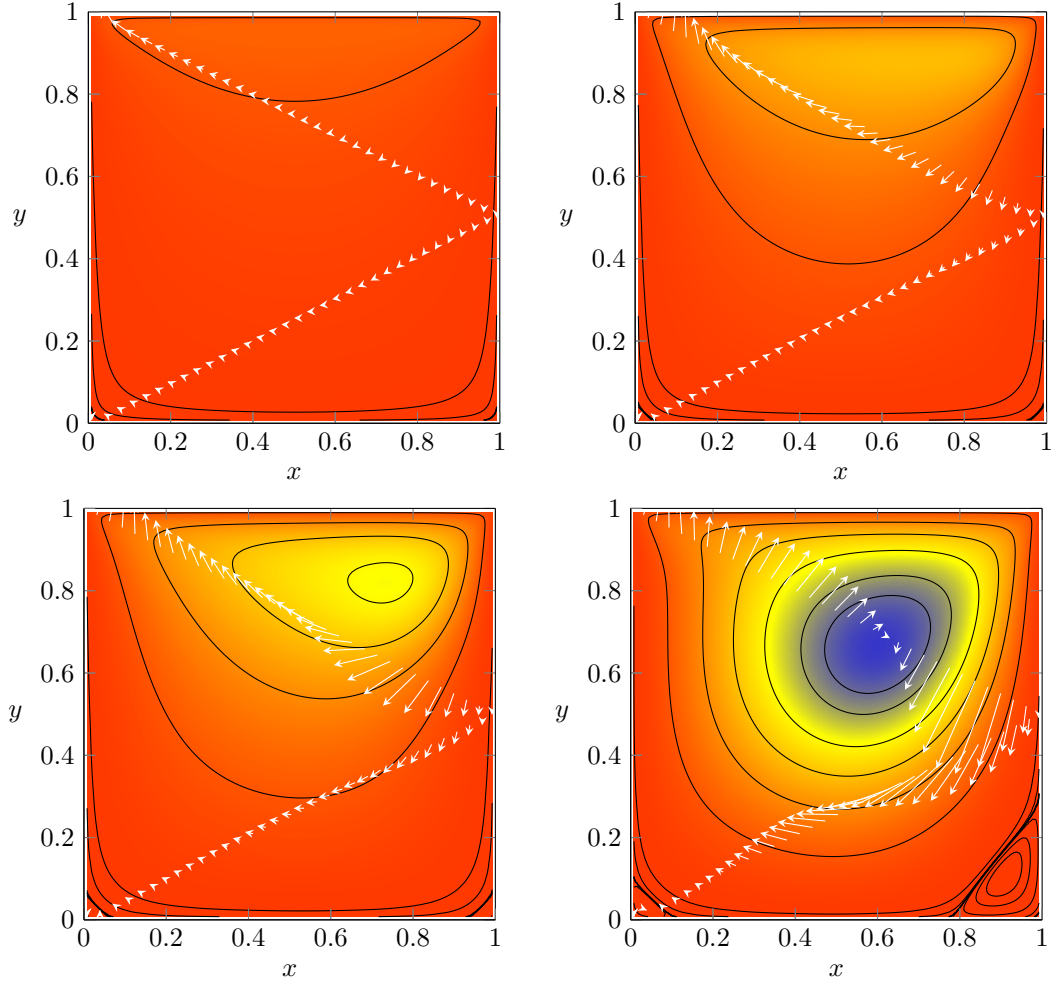


Figure 6: Transient results for $\text{Re} = 200$, $N = 129$ at different times: $t = 0.04$ (upper left), $t = 0.60$ (upper right), $t = 1.61$ (lower left) and $t = 10$ (lower right). The surface plots exhibit the stream function ψ , its contours are stream lines, and the vectors correspond to the velocity field \mathbf{u} at selected points of the domain.

grid sizes as we have considered (N up to 129) and $\text{Re} \leq 1000$. Although we concentrate on the cases where $\text{Re} \leq 1000$, it is naturally desirable for the code to work for as high Re as possible. For larger Reynolds numbers, we therefore employ $\Delta t = 100\Delta x/\text{Re}$, which works (at least) up to $N = 129$, $\text{Re} = 3200$.

3.2. Transient behaviour

In order to investigate how the impulsively started system evolves to steady-state, we initiated a test case with $\text{Re} = 200$ and $N = 129$, outputting the system state at even intervals. Figure 6 shows the state of the system at four different times through plots of the stream function and velocity vectors.

The system behaves as one would expect. Initially, the fluid is at rest in all parts of the domain. In the upper left plot of Figure 6, the system has only just started to be affected by the movement of the lid: there is a flow along the lid and a slight circulation from the upper right corner, through the center, and back to the upper left corner. In the next snapshot (upper right), this circulation has become more pronounced, as is evident from the relative size of the velocity vectors. In the lower left plot, the formation of a vortex is evident in the upper right corner. Finally, at steady-state (lower right), the system has evolved to its final configuration, where a constant circulation is present in the cavity, and we can even discern the creation of a sec-

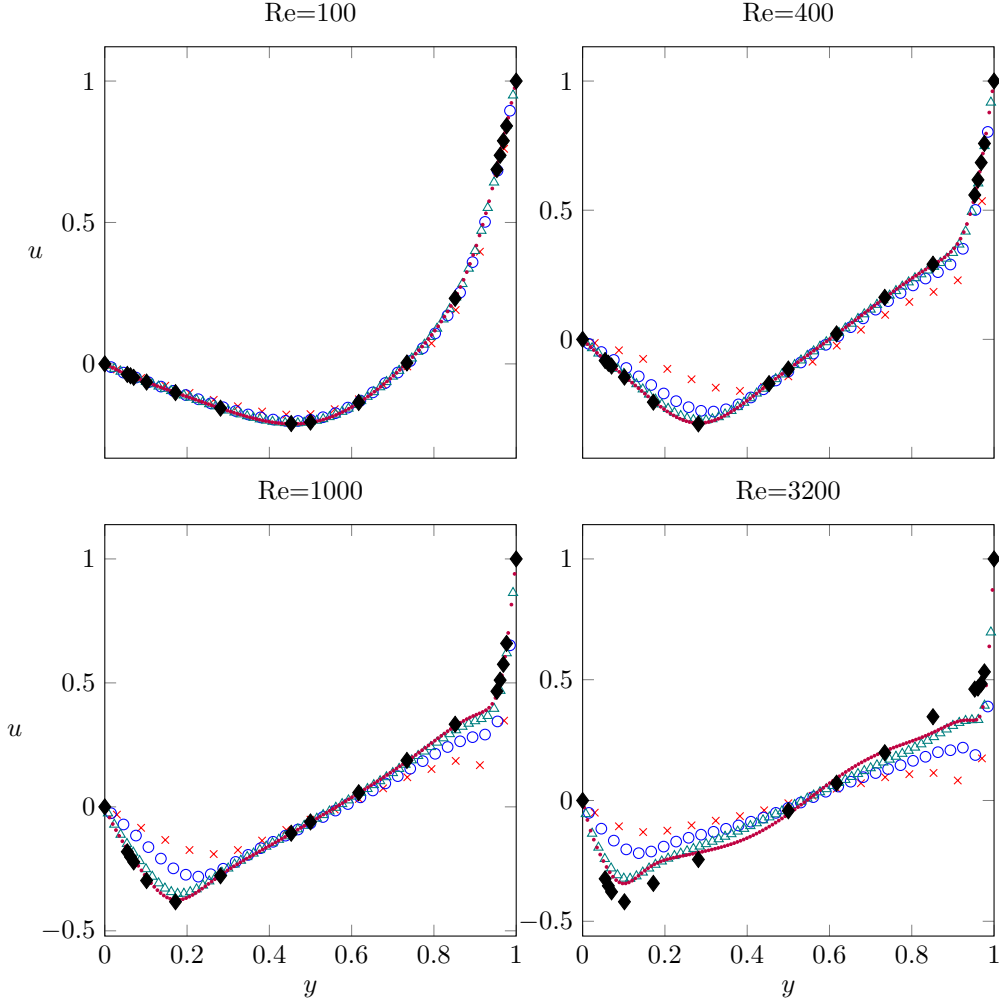


Figure 7: First component u of velocity through the slice $x = 0.5$. The filled black diamonds corresponds to tabulated results from Ghia et al.^[16]. \times $N = 17$, \circ $N = 33$, \triangle $N = 65$, \cdot $N = 129$.

ondary eddy in the lower right corner. Note that all the velocity vectors are parallel to the stream lines, as expected.

3.3. Steady-state solution

Known reference solutions are also necessary to validate the code. As such, we compare our findings with those of Ghia et al.^[16], since their paper is widely recognized as the reference for high-Re incompressible flow in the lid-driven cavity test case. Results have been computed with Reynolds numbers of 100, 400, 1000 and 3200 and grid sizes increasing from $N = 17$ to $N = 129$. In Figures 7 - 10, results are presented which visualize the steady-state distribution of velocities, stream function and vorticity.

Figure 7 shows how the first component of the velocity, u , varies in the plane $x = 0.5$, a slice through the geometric centre of the computational domain. Note especially the filled, black diamonds, which correspond to values tabulated by Ghia et al. in their paper^[16]. For $Re = 100$, our results are very close to the reference even for the smallest grid sizes. Our solver struggles more as Re increases, but it is still evident that grid refinement gives convergence. For the highest grid resolution, our results align perfectly with the reference for $Re \leq 1000$, and they even approach the reference solution for $Re = 3200$. Similar results for the second velocity component, v , are given in Figure 8. Here, the slice is through $y = 0.5$. We observe that the results tend

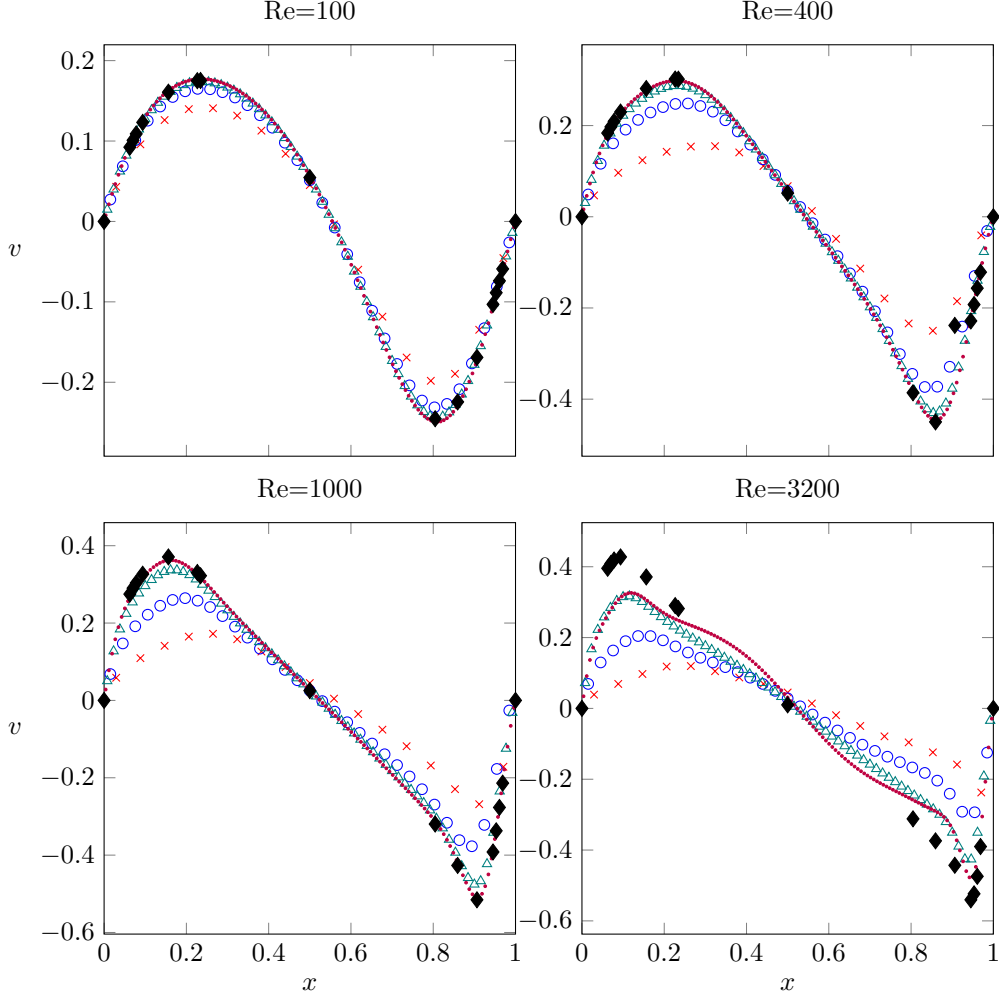


Figure 8: Second component v of velocity through the slice $y = 0.5$. The filled black diamonds corresponds to tabulated results from Ghia et al.^[16]. \times $N = 17$, \circ $N = 33$, \triangle $N = 65$, \cdot $N = 129$.

towards the reference solutions in the same manner as for u .

Figure 9 shows the distribution of the stream function and velocity field at steady-state. When compared to Figure 3 in the paper by Ghia et al. we see that the streamline pattern is near identical for all cases. The stream lines which we have plotted as contours of ψ are the same as those used in the reference. Our inclusion of the velocity field at selected places in the domain is merely to give an intuitive understanding of the distribution of flow. As the Reynolds number gets larger, we observe that the secondary eddies become more prominent, in agreement with our expectations from the literature. Figure 10 depicts the vorticity distribution in the domain, including contours. Our results are in-

distinguishable from the results as shown in Figure 4 in the reference^[16].

3.4. Computational efficiency

Since computational efficiency is an important factor in our ability to simulate realistic scenarios, it is beneficial to evaluate the performance of the code. For each pair of parameters Re and N , Table 1 contains the total runtime of the code in seconds, the number of iterations required to satisfy the steady-state tolerance and the runtime per iteration. The latter is computed by timing the while-loop only and dividing the result by the iteration count.

As is evident, the runtime quickly blows up as the Reynolds number and amount of grid points

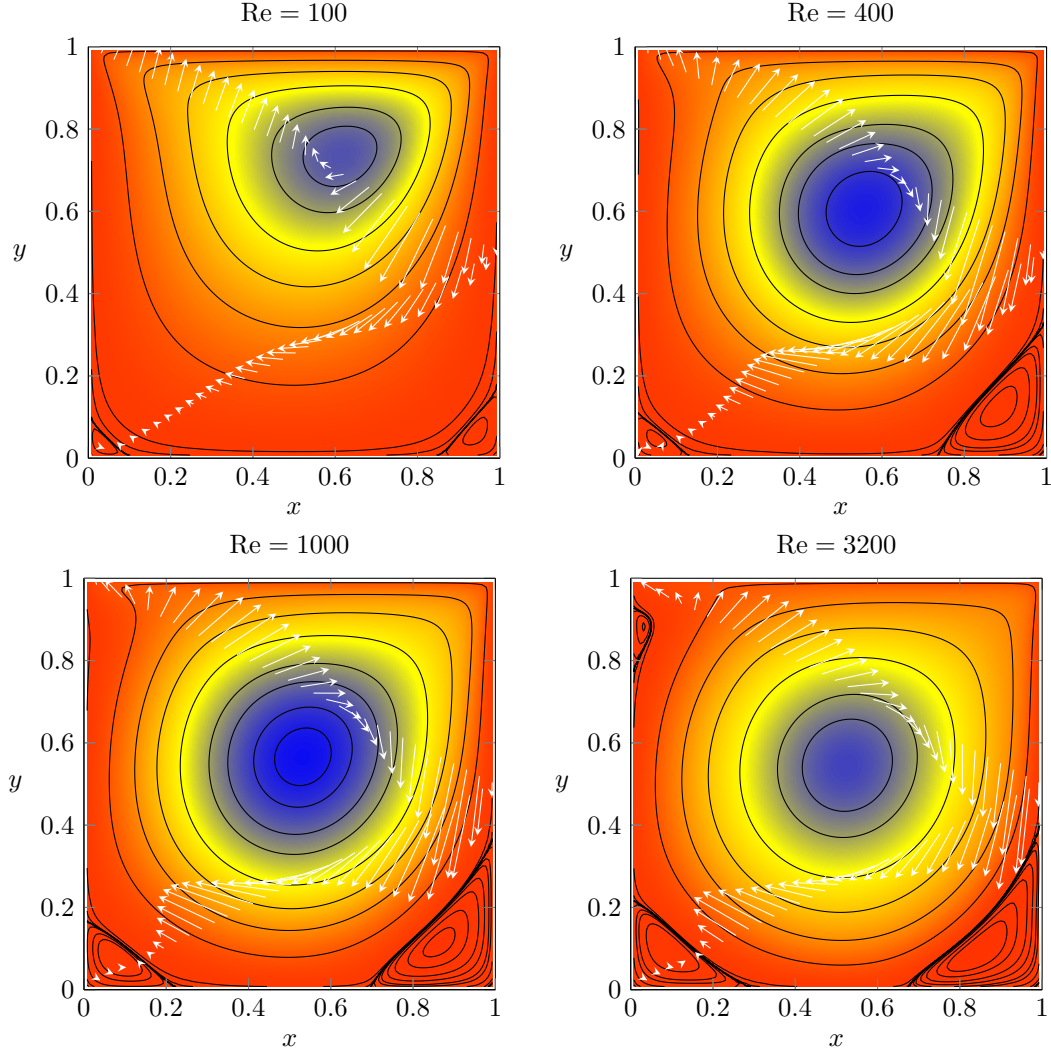


Figure 9: Surface plot of the stream function ψ for several different Reynold's numbers. The stream lines are the contours of ψ used in the reference by Ghia et al.^[16] Also plotted are selected vectors from the computed velocity field.

both increase. For the highest combination run, the simulation took just over two hours in total. Both parameters are inversely proportional to our choice of time step, so more iterations are needed to reach the same time. Additionally, the total time required to reach steady-state increases with Re . There is not, however, very much to be done computationally about these problems, except perhaps finding a choice of time step which is more optimally chosen as the largest permissible. The average time per iteration, on the other hand, is determined solely by the choice of spatial accuracy. Comparing the average runtime per iteration for different values of N , we note that it is approximately of the order $\mathcal{O}(N^2)$,

i.e. linear in terms of the matrix sizes for the systems being solved. This is as good as we can hope for for the problem of solving a system of equations given a decomposed matrix, and only possible since the matrices are sparse block-tridiagonal in nature.

4. Suggestions for further work

The most obvious next step is to implement the SIMPLE algorithm for solving the steady-state Navier-Stokes equations for Bingham plastics. This implementation is not necessarily trivial, especially if trying to do so in a computationally optimal manner, taking advantage of preconditioners and utiliz-

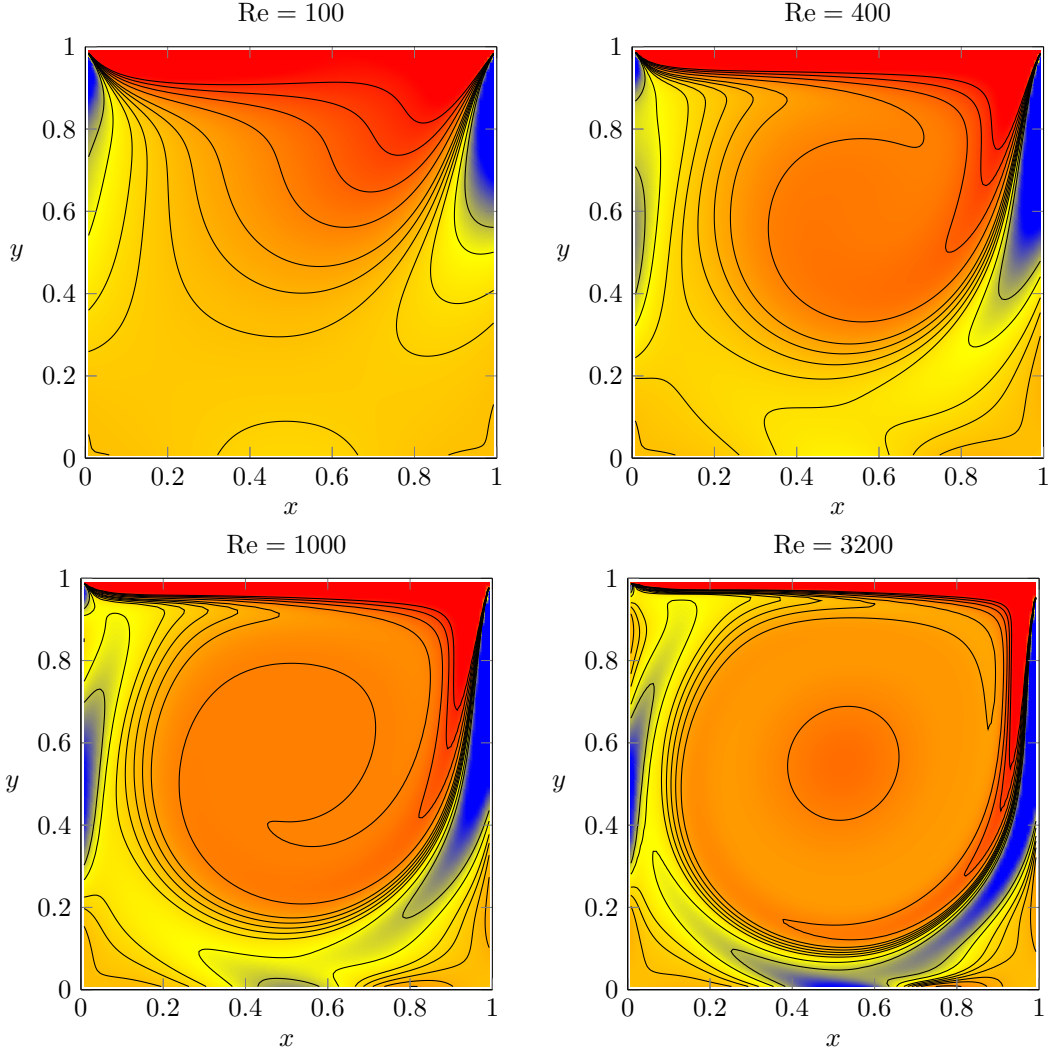


Figure 10: Surface plot of the vorticity ω for several different Reynold's numbers. The contour lines are the same as those used in the reference by Ghia et al. ^[16]

ing multigrid methods. It would also be very interesting to try and develop a transient solver of the same type as we have implemented for the Newtonian case, following the idea of semi-implicit temporal discretization of the viscous term.

For high Reynolds numbers, use of the time-marching PDE solver becomes a very inefficient method to obtain steady-state solutions. Higher grid sizes and smaller time steps are necessary for convergence, so obtaining results becomes impractical rapidly as Re is increased. For the steady-state case, one could use an algorithm such as SIMPLE or a vorticity-stream-function method. There are, however, actions that could be taken to speed

up the solver already implemented. Since each time step in the time-marching scheme is dependent on the previous one, optimization should be done within each time step. The matrices for the linear systems are only built once at the beginning of the simulation, and although the assembling of these could be looked into, the gain would probably be negligible compared to that achieved by speeding up the functions used within each time step.

We have not utilized proper vectorization when updating the load vectors for the linear systems, but instead calculated each component individually. This could perhaps reduce the time spent in each time step marginally, but the main computa-

Re	N	Runtime	Iter.	Time per iter.
100	17	0.09	58	$1.20690 \cdot 10^{-3}$
400	17	0.61	552	$1.08696 \cdot 10^{-3}$
1000	17	1.93	1710	$1.12881 \cdot 10^{-3}$
3200	17	29.9	26282	$1.13728 \cdot 10^{-3}$
100	33	0.67	99	$4.74747 \cdot 10^{-3}$
400	33	4.17	841	$4.73246 \cdot 10^{-3}$
1000	33	14.62	3035	$4.75124 \cdot 10^{-3}$
3200	33	154.02	32644	$4.71235 \cdot 10^{-3}$
100	65	6.05	174	$1.97126 \cdot 10^{-2}$
400	65	31.3	1385	$2.06426 \cdot 10^{-2}$
1000	65	88.99	4248	$2.01154 \cdot 10^{-2}$
3200	65	1226.28	60264	$2.03035 \cdot 10^{-2}$
100	129	68.45	308	$8.82792 \cdot 10^{-2}$
400	129	260.37	2412	$9.06758 \cdot 10^{-2}$
1000	129	680.18	7118	$8.97275 \cdot 10^{-2}$
3200	129	7289.88	81448	$8.90100 \cdot 10^{-2}$

Table 1: Total runtime, number of iterations required to reach steady-state and runtime per iteration for the various combinations of Re and N . The runtimes are measured in seconds.

tional effort is in solving the linear systems of equations. It would be difficult to improve on the actual solvers provided by the Eigen library (which, as we have seen, provide near-linear solving), but inspection of the (block) tridiagonal matrices make it apparent that they could be suitable for variants of the Hockney algorithm^[28], which decouples the system of equations to N diagonal systems, each easily solved rapidly (in $\mathcal{O}(N)$ operations). By utilizing the fast Fourier transform, the total computational complexity can be reduced to $\mathcal{O}(N \log N)$. Even further improvement could be possible by noting that the decoupled systems of equations enable parallelization.

Finally, steps should be taken to increase the amount of interesting systems we can look at. Inclusion of arbitrarily shaped domains can be done by using adaptive mesh refinement^[29,30] coupled with e.g. level set and ghost fluid methods^[29] or Cartesian cut cells^[31], which would also allow for moving boundaries. Additionally, extensions to three dimensions would be natural.

5. Conclusions

We have successfully implemented a numerical solver for Newtonian fluids obeying the unsteady, incompressible Navier-Stokes equations in two spatial dimensions. Our results for the benchmark

problem of a lid-driven cavity are in agreement with those previously presented in the literature for Reynolds numbers at least up to 3200, although computations converge slower and become more expensive quickly as Re increases. In addition to this implementation, we have discussed possible extensions to the special class of Non-Newtonian fluids known as Bingham plastics in the case of Reynolds number zero (creeping flow). There is nothing novel about the methods employed and the resulting code, but this project report nevertheless serves as a literature review which covers an introduction to the problem at hand, and which validates the robustness of our code through well-documented tests.

References

- [1] J. Marshall, A. Adcroft, C. Hill, L. Perelman, C. Heisey, A finite-volume, incompressible Navier-Stokes model for studies of the ocean on parallel computers, *Journal of Geophysical Research: Oceans* 102 (C3) (1997) 5753–5766.
- [2] F. X. Giraldo, M. Restelli, A study of spectral element and discontinuous Galerkin methods for the Navier-Stokes equations in nonhydrostatic mesoscale atmospheric modeling: Equation sets and test cases, *Journal of Computational Physics* 227 (8) (2008) 3849–3877.
- [3] M. M. Rai, Navier-Stokes simulations of rotor/stator interaction using patched and overlaid grids, *Journal of Propulsion and Power* 3 (5) (1987) 387–396.
- [4] J. L. Thomas, W. K. Anderson, S. T. Krist, Navier-Stokes computations of vortical flows over low-aspect-ratio wings, *AIAA journal* 28 (2) (1990) 205–212.
- [5] A. Jameson, L. Martinelli, N. Pierce, Optimum aerodynamic design using the Navier-Stokes equations, *Theoretical and Computational Fluid Dynamics* 10 (1-4) (1998) 213–237.
- [6] C. S. Peskin, Numerical analysis of blood flow in the heart, *Journal of Computational Physics* 25 (3) (1977) 220–252.
- [7] M. Mihaescu, S. Murugappan, M. Kalra, S. Khosla, E. Gutmark, Large eddy simulation and Reynolds-averaged Navier-Stokes modeling of flow in a realistic pharyngeal airway model: An investigation of obstructive sleep apnea, *Journal of Biomechanics* 41 (10) (2008) 2279–2288.
- [8] J. Deiber, W. Schowalter, Flow through tubes with sinusoidal axial variations in diameter, *AIChE Journal* 25 (4) (1979) 638–645.
- [9] G. Vinay, A. Wachs, J.-F. Agassant, Numerical simulation of weakly compressible Bingham flows: the restart of pipeline flows of waxy crude oils, *Journal of non-newtonian fluid mechanics* 136 (2) (2006) 93–105.
- [10] M. B. Cardenas, D. T. Slottke, R. A. Ketcham, J. M. Sharp, Navier-Stokes flow and transport simulations using real fractures shows heavy tailing due to eddies, *Geophysical Research Letters* 34 (14).
- [11] F. Boyer, C. Lapuerta, S. Minjeaud, B. Piar, M. Quintard, Cahn–Hilliard/Navier–Stokes model for the simu-

- lation of three-phase flows, *Transport in Porous Media* 82 (3) (2010) 463–483.
- [12] C. L. M. H. Navier, Memoire sur les lois du mouvement des fluides, *Mémoires de l'Académie Royale des Sciences de l'Institut de France* 6 (1822) 389–440.
 - [13] G. G. Stokes, On the theories of the internal friction of fluids in motion and of the equilibrium and motion of elastic solids, *Transactions of the Cambridge Philosophical Society* 8 (1845) 287–319.
 - [14] C. L. Fefferman, Existence and smoothness of the Navier-Stokes equation, *The Millennium Prize Problems* (2006) 57–67.
 - [15] E. C. Bingham, An investigation of the laws of plastic flow, *Bulletin of the Bureau of Standards* 13 (2) (1916) 309–353.
 - [16] U. Ghia, K. N. Ghia, C. Shin, High-Re solutions for incompressible flow using the Navier-Stokes equations and a multigrid method, *Journal of computational physics* 48 (3) (1982) 387–411.
 - [17] O. Zikanov, *Essential Computational Fluid Dynamics*, John Wiley & Sons, 2010.
 - [18] A. J. Chorin, Numerical solution of the Navier-Stokes equations, *Mathematics of Computation* 22 (104) (1968) 745–762.
 - [19] J.-G. Liu, Projection method I: convergence and numerical boundary layers, *SIAM journal on numerical analysis* 32 (4) (1995) 1017–1057.
 - [20] G. Guennebaud, B. Jacob, et al., *Eigen v3*, <http://eigen.tuxfamily.org> (2010).
 - [21] W. Kress, P. Lötstedt, Time step restrictions using semi-explicit methods for the incompressible Navier-Stokes equations, *Computer Methods in Applied Mechanics and Engineering* 195 (33) (2006) 4433–4447.
 - [22] D. Vola, L. Boscardin, J. Latché, Laminar unsteady flows of Bingham fluids: a numerical strategy and some benchmark results, *Journal of Computational Physics* 187 (2) (2003) 441–456.
 - [23] L. Muravleva, Uzawa-like methods for numerical modeling of unsteady viscoplastic Bingham medium flows, *Applied Numerical Mathematics* 93 (2015) 140–149.
 - [24] E. Mitsoulis, T. Zisis, Flow of Bingham plastics in a lid-driven square cavity, *Journal of Non-Newtonian Fluid Mechanics* 101 (1) (2001) 173–180.
 - [25] A. Syrakos, G. C. Georgiou, A. N. Alexandrou, Solution of the square lid-driven cavity flow of a Bingham plastic using the finite volume method, *Journal of Non-Newtonian Fluid Mechanics* 195 (2013) 19–31.
 - [26] A. Syrakos, G. C. Georgiou, A. N. Alexandrou, Performance of the finite volume method in solving regularised Bingham flows: Inertia effects in the lid-driven cavity flow, *Journal of Non-Newtonian Fluid Mechanics* 208 (2014) 88–107.
 - [27] T. C. Papanastasiou, Flows of materials with yield, *Journal of Rheology* 31 (5) (1987) 385–404.
 - [28] R. W. Hockney, A fast direct solution of Poisson's equation using Fourier analysis, *Journal of the Association for Computing Machinery (JACM)* 12 (1) (1965) 95–113.
 - [29] S. Schoch, K. Nordin-Bates, N. Nikiforakis, An Eulerian algorithm for coupled simulations of elastoplastic-solids and condensed-phase explosives, *Journal of Computational Physics* 252 (2013) 163–194.
 - [30] S. Lovett, N. Nikiforakis, F. Monmont, Adaptive mesh refinement for compressible thermal flow in porous media, *Journal of Computational Physics* 280 (2015) 21–36.
 - [31] R. Klein, K. Bates, N. Nikiforakis, Well-balanced compressible cut-cell simulation of atmospheric flow, *Philosophical Transactions of the Royal Society of London A: Mathematical, Physical and Engineering Sciences* 367 (1907) (2009) 4559–4575.